Contents

1. Introduction i

1.1 Background 1

1.2 Previous studies 2

1.3 Counter-flow jet 5

1.4 Objectives 6

2. Numerical method 7

2.1 Numerical schemes 7

2.1.1 Governing equation 7

2.1.2 Transport properties 8

2.1.3 Turbulence modeling 9

2.1.4 Spatial discretization 11

2.1.5 Temporal discretization 12

2.1.6 Runge-Kutta method 13

2.2 Numerical set-up 14

2.2.1 Physical model 14

2.2.2 Mesh generation 15

2.2.3 Boundary condition 16

2.2.4 Initial condition 18

2.2.5 Momentum parameter ratio (MPR) 19

3. Result & Discussion 20

3.1 Numerical validation 20

3.1.1 Numerical simulation on blunt body 20

3.1.2 Numerical simulation for counter-flow jet 21

3.1.3 Grid dependence 24

3.2 Effect of pressure conditions of the jet 25

3.2.1 Flow features and flow field 26

3.2.2 Analysis 34

3.3 Effect of exit Mach number 36

3.3.1 Flow features and flow field 38

3.3.2 Analysis 39

3.4 Effect of jet species 40

3.4.1 Flow features and flow field 41

3.4.2 Analysis 43

4. Conclusion 44

5. References 45

초 록 47

List of figures

Fig. 1 The Apollo capsule during atmospheric re-entry 1

Fig. 2 Flow features of aero-spike 3

Fig. 3 Flow features of counter-flow jet 3

Fig. 4 Flow features of laser energy deposition 4

Fig. 5 Schematic representation of the flow field features around the blunt body ..14

Fig. 6 Mesh generation 15

Fig. 7 Boundary condition 16

Fig. 8 Numerical simulation for blunt body (a) Previous study (b) Present numerical result 20

Fig. 9 Local density gradient for LPM (a) Present numerical research (b) Previous study 22

Fig. 10 Local density gradient for SPM (a) Present numerical research (b) Previous study 23

Fig. 11 Grid dependence test of nodes=60000 24

Fig. 12 Analysis of the flow field at LPM (a) Present numerical result (b) Previous study 27

Fig. 13 NPR=0.20 at 1.28ms (a) Local density gradient (b) Pressure contour 28

Fig. 14 NPR=0.40 at 0.69ms (a) Local density gradient (b) Pressure contour 29

Fig. 15 NPR=0.75 at 0.69ms (a) Local density gradient (b) Pressure contour 29

Fig. 16 Analysis of the flow field at SPM (a) Present numerical result (b) Previous study 31

Fig. 17 NPR=1.05 at 0.38ms (a) Local density gradient (b) Pressure contour 32

Fig. 18 NPR=1.20 at 0.52ms (a) Local density gradient (b) Pressure contour 32

Fig. 19 NPR=1.50 at 0.49ms (a) Local density gradient (b) Pressure contour 33

Fig. 20 Total pressure coefficient according to the NPR.....34

Fig. 21 Wall pressure distribution along the blunt body.....35

Fig. 22 Local density gradient at higher Mach number of jet (a) SPM at NPR=0.40 (b) LPM at NPR=1.05 38

Fig. 23 Drag coefficient for lower Mach number and higher Mach number.....39

Fig. 24 Local density gradient with different gases (a) Argon (b) Carbon dioxide (c) Air 42

Fig. 25 Drag coefficient with different gas species……43

List of tables

Table 1 Flow conditions of free-stream and jet condition with air 26

Table 2 Parameters of jet 37

Table 3 MPR at different Mach number 37

Table 4 Jet flow conditions with different species of jet.....41

Abstract

Numerical investigation of counter-flow jet on a hypersonic blunt body for drag reduction

Hee Yoon
Department of Mechanical and Aerospace Engineering
The Graduate school
Seoul National University

A numerical investigation has been conducted for drag reduction of a blunt body with a counter flow jet at Mach number 6. The computational study was carried out by solving axisymmetric, explicit, Reynolds Averaged Navier-Stokes (RANS) equations. Spalart-Allmaras one equation are used for turbulence model. By releasing a jet into the air, the shock structure is changed from bow shock wave to multiple shock structure. Ultimately, the changed shock structure leads to drag reduction. The purpose of this study is to investigate the influence of the stagnation pressure, exit Mach number and gas species of the jet based on the parameters of momentum parameter ratio (MPR) of jet. The results show that the flow-field can be categorized long penetration mode (LPM) and short penetration mode (SPM)

depending on the penetration length of jet. In LPM, the shock structure is continuously fluctuated so that the flow field is unstable. Therefore, even if the penetration length of jet is very long, the drag cannot be reduced significantly. On the other hand, at SPM, the shock structure is almost fixed and the entire flow field is stable. Therefore, even if the penetration length is short, the drag can be reduced by up to 40%. In conclusion, high pressure, high Mach number, and high molecular weight of jet is beneficial for drag reduction.

Keywords : Hypersonic, counter-flow jet, drag reduction, Momentum parameter ratio (MPR)

Student Number : 2015-20783

1. Introduction

1.1 Background

As the aeronautical techniques are developed, hypersonic flight is possible. Hypersonic flow means that the Mach number is greater than 5. Hypersonic flow is important because it is physically different from supersonic flow and it is the flow that will dictate many of the new aerodynamic vehicle designs for the 21st century. A hypersonic vehicle can be an airplane, missile, or spacecraft. Some hypersonic vehicles have a special type of jet engine called a supersonic combustion ramjet or scramjet to fly through the atmosphere. Sometimes, a hypersonic plane uses a rocket engine. A re-entry vehicle is another type of hypersonic vehicle such as Apollo re-entry capsule as shown in Fig. 1.

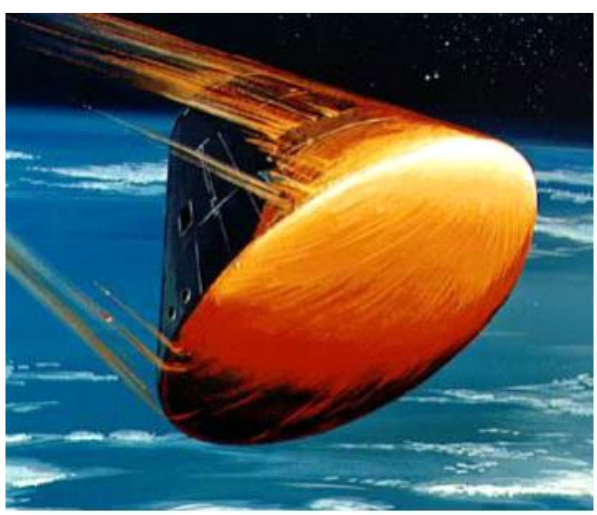

Fig. 1 The Apollo capsule during atmospheric re-entry

The most serious problem for hypersonic vehicles is the strong shock wave is formed in front of the vehicle's nose that creates high temperature and high pressure condition known as aerodynamic drag. For example, the temperature in the nose region of a hypersonic vehicle can be extremely reaching approximately 11000K at Mach number 36 and amount of aerodynamic drag is applied on the vehicle's body. As the drag is one of the most important factors on vehicle performances and vehicle design process, it is necessary to reduce the drag forces.

1.2 Previous studies

Since 1950s, many researchers have been interested in the application of flow control methods to modify or change the external flow field of vehicles in order to reduce the drag component [1-9]. The methods can be categorized passive flow control and active flow control. Passive control solution is to install the rod or spike in front of the body. Therefore, external energy or mass injection to the flow field is unnecessary. It mainly changes or modifies the geometry of the vehicle and affects the certain flow environment such as boundary conditions and pressure gradient. The one of examples of passive flow control is aero-spike as shown in the Fig. 2. In 1959, Bodonoff, S. N and Vas, L. E conducted experimental researches on drag reduction with aero-spike [8].

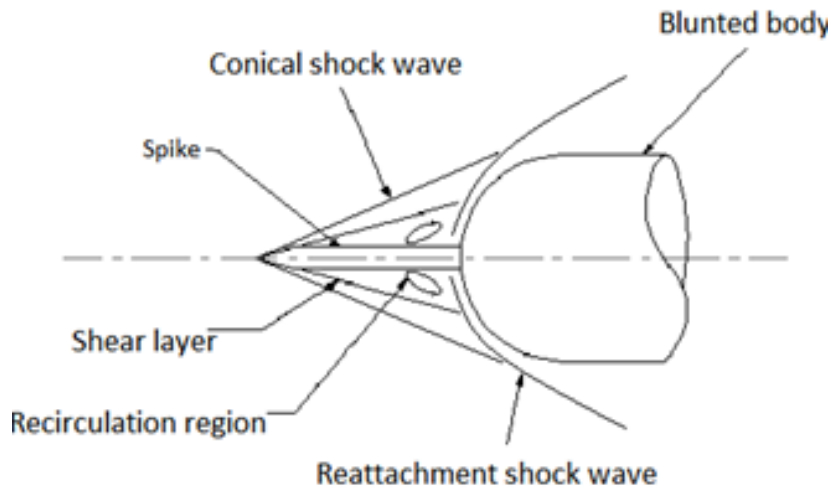

Fig. 2 Flow features of aero-spike

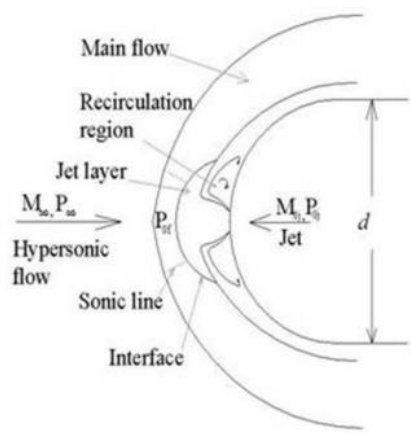

Fig. 3 Flow features of counter-flow jet

On the other hand, active flow control is injecting energy or external power into the flow that modifies the energy deposition alongside the vehicle body. Fig. 3 represents the example of active flow control, counter-flow jet [4]. Counter-flow jet releases gas into the free-stream flow. In 1960s, Finley, P. J experimentally investigated counter-flow jets in a Mach 2.5 free-stream using two jet nozzles. He classified the flow field around a blunt body with a counter-flow jet into three conditions, namely steady, unsteady, and transitional [1].

According to the studies of Feszty, D., Badcock, K. J., K, Richards, B. E. [2] and Panaras, A. G., and Drikakis, D.[3], the flow field condition is similar with aero-spike [2-3].

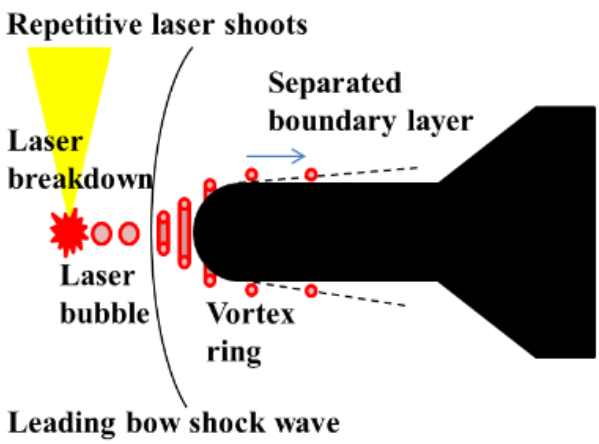

Fig. 4 Flow features of laser energy deposition

The another active flow control to reduce drag force is laser energy deposition method as shown in Fig. 4[9]. Osuka, T., et al. conducted experimental research with laser energy deposition to investigate drag reduction [9].

1.3 Counter-flow jet

Among several drag reduction techniques, the counter-flow jet technique has been considered the most promising technique to reduce the drag. There are three big problems when using the aero-spike at hypersonic flow.

One problem is the drag is inversely increasing because of the spike over the Mach number 3. Another problem is the drag and heat transfer rate are increasing to the vehicle body when angle of attack (AOA) is over the 15 degree. Lastly, the aero-spike's head tip is very small compared with the blunt body nose and the heat quantity is inversely linearized the radius of the nose. Therefore, when using the small tip of the spike, there are too many heat addition is applied to the blunt body so the spike tip is melted.

For these reasons mentioned above, many researchers have studied on the counter-flow jet. Moreover, because of the development of the space shuttle and re-entry vehicle, they have focused on the counter-flow jet. However, the interaction of the counter-flow jet with the bow shock is rather complex than aero-spike. Therefore, it is necessary to understand the mechanism of the counter-flow jet.

1.4 Objectives

From the 1960s, the flow field around a blunt body with counter-flow jet was categorized by Finley into three conditions, steady, unsteady and transitional [1]. These are observed same as around a blunt body by Shang, J. S et al. conducted experimental researches with counter-flow jet [5-7]. They investigated with different jet pressure condition and effect of exit Mach number of jet with various nozzle throat sizes. They also investigated the thermal effect at fixed jet pressure injection by changing the gas temperature of the jet [5-7]. However, from now, the explanation for flow field is not sufficient. Moreover, the researches related to different species of jet such as monatomic, diatomic, polyatomic species of jet have not been conducted.

Therefore, the purpose of this study is to investigate the counter-flow jets through numerical simulations with various jet pressure conditions so that to provide useful information to reduce the drag efficiently. In addition, exit Mach number of the jet effect is investigated at same nozzle throat and effect of jet species are studied at different gamma ratio of the jet.

2. Numerical method

2.1 Numerical schemes

2.1.1 Governing equation

The governing equations for this study are two-dimensional, explicit, compressible, Reynolds-averaged Navier-Stokes equations. The Navier-Stokes equations are used as the following:

Conservation of mass :

$$\frac{\partial \rho}{\partial t} + \nabla \cdot (\rho \vec{v}) = 0$$

Conservation of momentum :

$$\frac{\partial \rho \vec{v}}{\partial t} = \rho f + + \nabla \cdot (T - \rho \vec{v} \vec{v})$$

Conservation of energy :

$$\rho \frac{De}{Dt} + p \nabla \cdot \vec{v} = \Phi + \nabla \cdot k \nabla T$$

where $T = (-p + \lambda \nabla \cdot u)I + 2\mu D$, T represents stress tensor, D is strain rate, I is the identity matrix, μ is the coefficient of viscosity, $\lambda = -2/3\mu$. Because of the steady state, the time term can be ignored.

The simulation is solved by the finite volume method. The finite volume method is to satisfy the integral form of the conservation of mass, momentum and turbulent properties. For spatial discretization, explicit formulation with 4 stages Runge-Kutta equations are used and the first-order upwind scheme is used to discretize both momentum and continuity equations. The convective fluxes are simulated using the Advection Upstream Splitting method(AUSM) equations developed as a

numerical inviscid flux function for solving a general system of conservation equations. It is based on the upwind concept and is motivated to provide an alternative approach to other upwind methods, such as the flow difference splitting methods by ROE and Godunov method. In this thesis, it is necessary to investigate the shock condition so AUSM equations are used.

2.1.2 Transport properties

In this study, more than two species of gas are used. Therefore, it is necessary to consider mixing problem. Based on the ideal gas, the gas law can be expresses as like this :

$$\rho = \frac{P_{abs} + P}{RT\sum_i \frac{Y_i}{M_{w,i}}} \qquad C_{p,i} = \frac{1}{2}\frac{R}{M_{w,i}}(f_i + 2)$$

$$\mu = \sum_i \frac{X_i \mu_i}{\sum_j X_j \phi_{ij}}, \qquad \phi_{ij} = \frac{\left[1 + \left(\frac{\mu_i}{\mu_j}\right)^{1/2}\left(\frac{M_{w,j}}{M_{w,i}}\right)^{1/4}\right]^2}{\left[8(1 + \frac{M_{w,j}}{M_{w,i}})\right]^{1/2}}$$

f_i is the number of modes of energy storage for the gas species i Y_i is the mass fraction of species i, X_i is the mole fraction of i. In this paper, viscosity is expressed as a function of temperature by using Sutherland's law. The formula is specified using three coefficients.

Sutherland's law with three coefficients has the form

$$\mu = \mu_0 \left(\frac{T}{T_0}\right)^{3/2} \frac{T_0 + S}{T + S}$$

For air, $\mu_0 = 1.16 \times 10^{-5} \frac{\text{kg}}{\text{ms}}, T_0 = 273.15K.$

2.1.3 Turbulence modeling

To include the turbulence model, Spalart-Allmaras model is used. The Spalart-Allmaras model is a one equation model that solves a modeled transport equation for the kinematic eddy viscosity. The Spalart-Allmaras model was designed specifically for aerospace applications involving wall-bounded flows and has been shown to give good results for boundary layers subjected to adverse pressure gradients.

The transported variable in the Spalart-Allmaras model, $\tilde{v}$, is identical to the turbulent kinematic viscosity except in the near-wall region. The transport equation for $\tilde{v}$ is following :

$$\frac{\partial}{\partial t}(\rho\tilde{v}) + \frac{\partial}{\partial x_i}(\rho\tilde{v}u_i)$$

$$= G_v + \frac{1}{\sigma_{\tilde{v}}}\left[\frac{\partial}{\partial x_j}\{(\mu + \rho\tilde{v})\frac{\partial\tilde{v}}{\partial x_j}\} + C_{b2}\rho\left(\frac{\partial\tilde{v}}{\partial x_j}\right)^2\right] - Y_v + S_{\tilde{v}}$$

Where G_v is the production of turbulent viscosity, and Y_v occurs in the near wall region due to wall blocking and viscous damping, $\sigma_{\tilde{v}}$ and C_{b2} and v is the molecular kinematic viscosity. $S_{\tilde{v}}$ is a user-defined source term. The turbulent viscosity (μ_t) is computed from $\mu_t = \rho\tilde{v}f_{v1}$, where the viscous damping function (f_{v1}) is given by

$$f_{v1} = \frac{x^3}{x^3 + {C_{v1}}^3} \quad , \chi \equiv \frac{\tilde{v}}{v}$$

The production term(G_v) is modelded as

$$G_v = C_{b1}\rho\tilde{S}\tilde{v} \ , \quad \tilde{S} \equiv S + \frac{\tilde{v}}{k^2 d^2} f_{v2}, \quad f_{v2} = 1 - \frac{x}{1 + x f_{v1}}$$

C_{b1} and k are constants, d is the distance from the wall, and S is a scalar measure of the deformation tensor. S is based on the magnitude of the vorticity:

$\mathrm{S} \equiv \sqrt{2\Omega_{ij}\Omega_{ij}}$ where Ω_{ij} is the mean rate of radiation tensor and is defined by

$$\Omega_{ij} = \frac{1}{2}\left(\frac{\partial u_i}{\partial x_i} - \frac{\partial u_j}{\partial x_j}\right)$$

The justification for the default expression for S is that for shear flows, vorticity and strain rate are identical. Vorticity has the advantage of being aero in inviscid flow regions like stagnation lines, where turbulence production due to strain rate can be unphysical. In ANSYS FLUENT, an alternative formulation has been proposed. The modification combined the measures of both vorticity and the strain tensors in the definition of S :

$$\mathrm{S} \equiv |\Omega_{ij}| + C_{prod}\min(0, |S_{ij}| - |\Omega_{ij}|)$$

Where

$$C_{prod} = 2.0, \quad |\Omega_{ij}| \equiv \sqrt{2\Omega_{ij}\Omega_{ij}}, \quad |\mathrm{S}_{ij}| \equiv \sqrt{2S_{ij}\mathrm{S}_{ij}}$$

With the means strain rate (S_{ij})

$$\mathrm{S}_{ij} = \frac{1}{2}\left(\frac{\partial u_j}{\partial x_i} + \frac{\partial u_i}{\partial x_j}\right)$$

Including both the rotation and strain tensors reduces the production of eddy viscosity and consequently reduces the eddy viscosity itself in regions where the measure of vorticity exceeds that of strain rate.

2.1.4 Spatial discretization

In this paper, control volume based technique is used to convert a general scalar transport equation to an algebraic equation that can be solved numerically. This control volume technique consists of integrating the transport equation about each control volume, yielding a discrete equation that expresses the conservation law on a control-volume basis.

Discretization of the governing equations can be illustrated most easily by considering the unsteady conservation equation for transport of a scalar quantity ϕ. This is demonstrated by the following equation written in integral form for an arbitrary control volume V as follows :

$$\int_V \frac{\partial \rho \phi}{\partial t} dV + \oint \rho \phi \vec{v} \cdot d\vec{A} = \oint \Gamma_\phi \nabla \phi \cdot d\vec{A} + \int_V S_\phi \, dV$$

This equation is applied to each control volume, or cell in the computational domain. It can be expressed as follows:

$$\frac{\partial \rho \phi}{\partial t} V + \sum_f^{N_{faces}} \rho_f \vec{v}_f \phi_f \cdot \vec{A}_f = \sum_f^{N_{faces}} \Gamma_\phi \nabla \phi \cdot \vec{A}_f + S_\phi \mathrm{V}$$

This equation must be interpolated from the cell center values. This is accomplished using an upwind scheme.

In this thesis, first-order upwind scheme is used. It means that quantities at cell faces are determined by assuming that the cell-center values of any field variable represent a cell-averaged value and hole throughout the entire cell. The face quantities are identical to the cell quantities. Moreover, the face value ϕ_f is set equal to the cell-center value of ϕ in the upstream cell.

2.1.5 Temporal discretization

A generic expression for the time evolution of a variable ϕ is given as bellows :

$$\frac{\partial \phi}{\partial t} = F(\phi)$$

In this study, density-based explicit formulation is used. Explicit time integration means that $F(\phi)$ is evaluated as follows

$$\frac{\phi^{n+1} - \phi^n}{\Delta t} = \mathrm{F}(\phi^n)$$

And

$$\phi^{n+1} = \phi^n + \Delta t F(\phi^n)$$

Here, the time step Δt is limited by the Courant-Friedrichs-Lewy condition(CFL condition). In addition, 4-stage Runge-Kutta scheme is used for unsteady flows. In the explicit scheme a multi-stage, time-steeping algorithm is used to discretize.

2.1.6 Runge-Kutta method

Runge-Kutta methods can be classified as implicit or explicit iterative methods. It is used in temporal discretization for the approximate solutions of ordinary differential equations. In this thesis, RK4, classical Runge-kutta method is used.

Let's symbolize that a given vector y and the vector is function of time t_n. The rate at which y changes $\acute{y}$ is a function of t and of y itself. At the initial time t_0, it can be written as :

$$\acute{y} = f(t, y), \qquad y(t_0) = y_0$$

$$y_{n+1} = y_n + h\sum_{i=1}^{s} b_i k_i$$

Here, k_i

$$k_1 = f(t_n, y_n)$$

$$k_2 = f\big(t_n + c_2 h, y_n + h(a_{21}k_2)\big)$$

$$k_3 = f\big(t_n + c_3 h, y_n + h(a_{31}k_1 + a_{32}k_2)\big)$$

$$\vdots$$

$$k_s = f\left(t_n + c_s h, y_n + h\big(a_{s1}k_1 + a_{s2}k_2 + \cdots + a_{s,s-1}k_{s-1}\big)\right)$$

Therefore, the four-stage Runge-Kutta method is given by :

$$y_{n+1} = y_n + \frac{h}{6}(k_1 + 2k_2 + 2k_3 + K_4)$$

2.2 Numerical set-up

2.2.1 Physical model

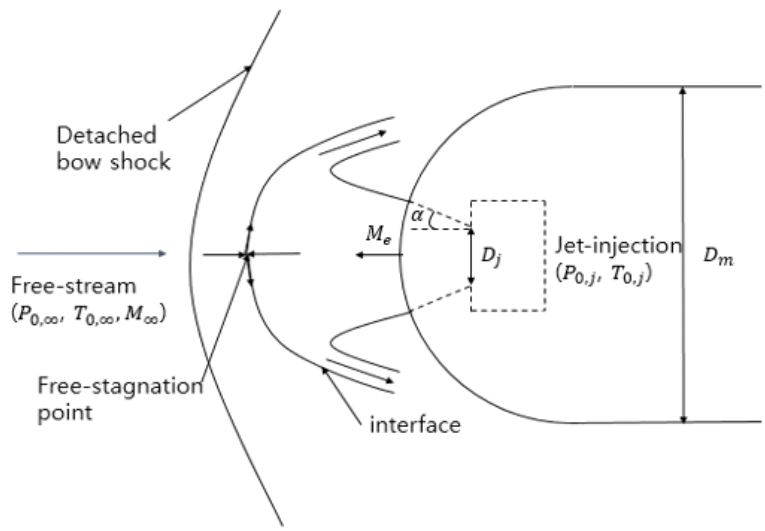

Fig. 5 Schematic representation of the flow field features around the blunt body

A two dimensional axisymmetric configuration was considered for the numerical model. The geometries are obtained from major reference [5-7]. As shown in the Fig. 5, the counter-flow jet interacts with the free-stream of the flow and forms new displacement shape to the blunt body. Based on the previous studies [1-4], the jet nozzle diameter is 2.44mm and the blunt body nose diameter (D_m) is 76.2mm. The jet exit diameter is 4.7, 5.35mm. The jet exit Mach number is 2.86, 3.13 respectively and conical nozzle expansion angle (α) is 4° The mass flow rate of the jet ranges from 1.52g/s to 7.60g/s. The opposing jet species are air, carbon dioxide and argon.

The jet stagnation temperature ($T_{0,j}$) is 294K and the jet stagnation pressure ($P_{0,j}$) is varied from 0 to 1Mpa if the opposing jet is the air. At different species of the jet such as carbon dioxide and argon, the jet stagnation pressure is 689Kpa. For free-stream conditions, the stagnation pressure of the flow field ($P_{0,\infty}$) is 689Kpa. The Mach number of free-stream (M_{∞}) is 6. NPR denotes jet total pressure ratio ($P_{0,j}/P_{0,\infty}$) and it ranges from 0 to 1.5.

2.2.2 Mesh generation

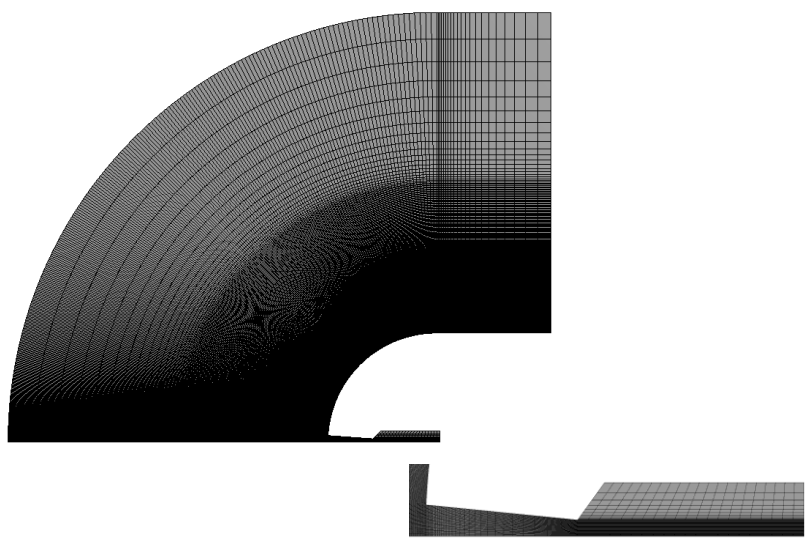

Fig. 6 Mesh generation

In order to generate the mesh to solve the numerical research, ANSYS FLUENT mesh CFD generation tool is used in this paper. The computation domain and detailed structured mesh grid is shown in Fig. 6. The numerical domain is divided with 9 zones to effectively generate the mesh. Before deciding the number of nodes, grid dependence experiments are conducted. From the grid dependence numerical simulations, over the 100000 nodes are effective to investigate the flow field and catch the shock wave. As a result, the total number of nodes is 114976 and total elements are 114219. In addition, as the flow field is continuously changed and the mesh grid elements are influenced to the numerical result near the exit nozzle area, the first mesh thickness is 50μm in order to catch the shock wave.

2.2.3 Boundary condition

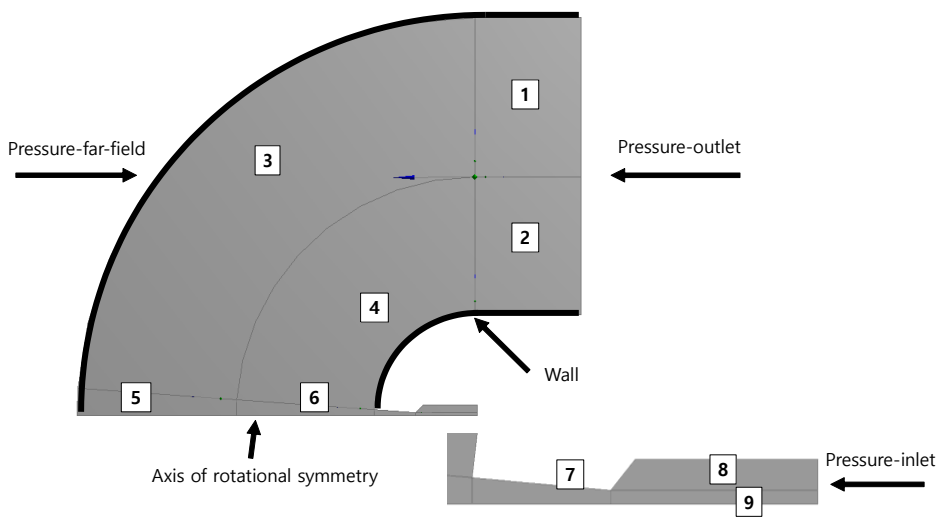

Fig. 7 Boundary condition

Boundary conditions consist of pressure inlet, pressure-outlet, pressure far-field, wall conditions as shown in the Fig. 7. Pressure inlet boundary conditions are used to define the fluid pressure at flow inlets, along with other scalar properties of the flow.

Pressure inlet boundary conditions can be used when the inlet pressure is known but the flow rate and velocity is unknown. Based on the previous study [5-7], the pressure inlet cases are known. In the pressure inlet boundary condition, it is necessary to decide static pressure and dynamic pressure. Supersonic/initial Gauges pressure is the static pressure. In this paper, the velocity of the nozzle chamber is zero, so the static pressure is same as total pressure condition.

Moreover, the flow direction is defined as a unit vector ($\vec{d}$), which is aligned with the local velocity vector ($\vec{v}$). This can be simply as

$$\vec{d} = \frac{\vec{v}}{|v|}$$

When using ANSYS FLUENT, it is unnecessary to input unit vector.

Pressure-outlet boundary conditions require the specification of a static pressure at the outlet boundary. However, the static pressure at the outlet boundary is unknown and it is impossible to predict the pressure condition. Therefore, non-reflecting boundary condition (NRBC) is used. This condition is needed to avoid false reflection.

In addition, pressure far-field conditions are used to model a free-stream condition at infinity, with free-stream Mach number and static condition being specified. The static pressure, static temperature and Mach number of the free-stream flow is

decided. Furthermore, the flow direction can be defined at a pressure far-field boundary conditions. As the geometry is 2D axisymmetric, axial, radial and tangential, component of flow direction information is necessary.

Lastly, the wall boundary condition is also decided in this paper. Wall boundary conditions are used to bound fluid and solid regions. At wall boundary condition, the no-slip boundary condition is enforced at walls.

2.2.4 Initial condition

It is necessary to define the starting positions, velocities and other parameters before starting CFD simulations. Initial guess condition values should be provided to solve the flow field and obtain desired final solution.

In ANSYS FLUENT, there are two methods for initializing the solution. However, in this paper, standard initialization method is used as the initialization method.

To initialize the flow field, pressure-far-field zone is selected as the reference value. Before initializing, patching function should be used. It should be done to patch different values for particular zones in the nozzle chamber. At the nozzle chamber, the velocity of the chamber should be zero. Moreover, at the nozzle chamber, the temperature of the chamber should be same as the boundary condition of pressure-inlet conditions.

2.2.5 Momentum parameter ratio (MPR)

Momentum parameter ratio (MPR) is defined as shown in the following equation.

$$\text{MPR}=\frac{\gamma_j {M_j}^2 P_{o,j}}{\gamma_\infty {M_\infty}^2 P_\infty}\left(\frac{P_j}{P_{0,j}}\right)\left(\frac{A_j}{A_b}\right.$$

The MPR defined as where the subscripts ∞ and j refer to free-stream and jet conditions, respectively. The quantity M is the Mach number, P is the pressure, and A represents the reference areas (jet exit and blunt body base). The MPR is seen to be the ratio of momentum flow out of the jet to free-stream momentum across a surface whose area is equal to the blunt body base area [10]. Based on the MPR, the jet parameters are investigated.

3. Result & Discussion

3.1 Numerical validation

3.1.1 Numerical simulation on blunt body

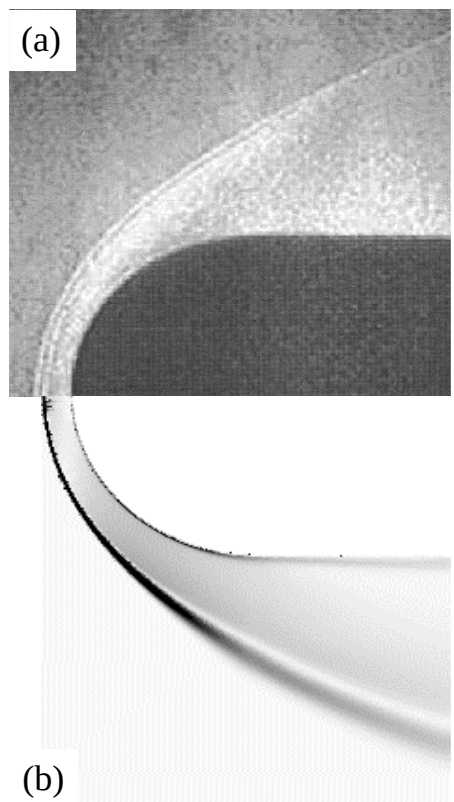

Fig. 8 Numerical simulation for blunt body (a) Previous study

(b) Present numerical result

In this paper, in order to simulate the counter-flow jet, computational simulation tool, ANSYS FLUENT ver.16.2 is used. Before calculating complex problems, it is necessary to validate the CFD tool. In order to validate the ANSYS FLUENT, numerical simulation on blunt body for without jet blowing is investigated to compare with the previous studies [5-7].

Depending on the vehicle's body shape, the shock stand-off distance is determined as shown in the Fig. 8 [11]. When the blunt body's radius is 76.2mm, theoretical shock stand-off distance is 5.873mm and the shock distance of calculated numerical validation result is 5.757mm. The shock distance is not perfectly fitted. However, the numerical error is 0.1mm so it could be said that the numerical tool is validated.

3.1.2 Numerical simulation for counter-flow jet

Firstly, it is necessary to validate complex flow field condition. Depending on penetration length of jet, the flow field can be categorized long penetration mode (LPM) and short penetration mode (SPM). In order to validate the computational tool, numerical simulation for counter-flow jet is conducted at different pressure ratio. In this paper, the pressure ratio is names as NPR defined by jet pressure to free pressure of free-stream flow and the simulations are conducted LPM when NPR is 0.75 and SPM when NPR is 1.05.

Fig. 9 shows local density gradient and the flow time of Fig. 9(a) is 7.611ms. In LPM, because the flow field is entirely very unstable and highly oscillates, it is very difficult and takes a long time to capture shock wave. However, as shown in Fig. 9, present numerical result is quite similar as the previous study [5-7].

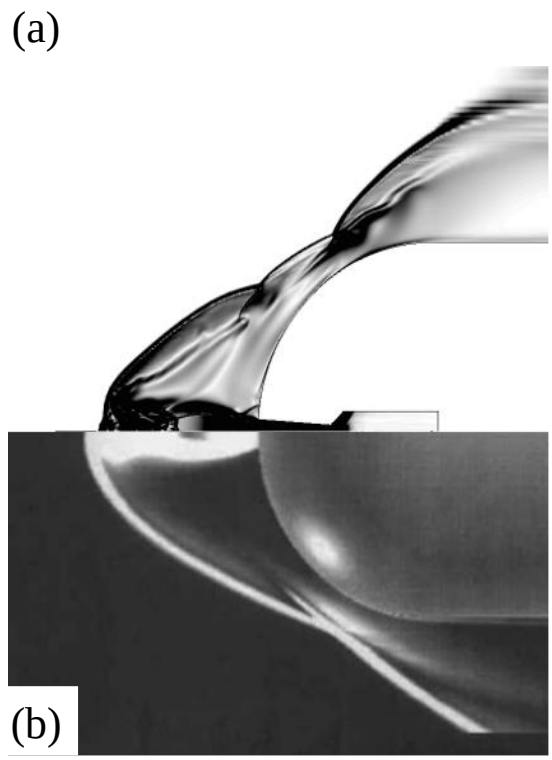

Fig. 9 Local density gradient for LPM (a) Present numerical research
(b) Previous study

.

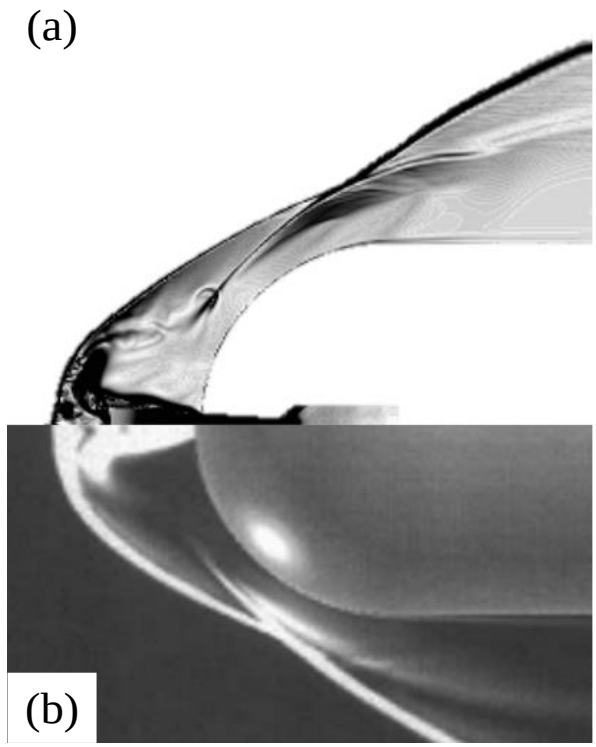

Fig. 10 Local density gradient for SPM (a) Present numerical research

(b) Previous study

Fig. 10 presents local density gradient for SPM and the flow time of Fig.10(a) is 2.811ms. Contrary to LPM, the flow field is stable at SPM. As a result, it can be easily capture the shock wave and present numerical research is same as previous study shown in the Fig. 10 [5-7].

From the simulations for LPM and SPM, numerical simulation tool is validated and it could be said the ANSYS FLUENT is believable. Therefore, from this validation, it is possible to change NPR to conduct other simulations.

3.1.3 Grid dependence

At first, in order to save the numerical research expenses, the mesh which does not effectively effect to the flow field was very coarse. As a result, the flow field does not exactly capture the shock wave and as shown in Fig. 11. In Fig. 11, the calculated pressure drag coefficient along the blunt body wall is 0.72 when the NPR 0.75.

In order to solve exactly, the mesh elements are increased to 114219. By increasing the X-directions especially wall distribution, the mesh is formed fine near the counter-flow nozzle and the coarse mesh is positioned on the radial direction as shown in the Fig. 6. The calculated drag coefficient is 0.714 when the NPR is 0.75. From this calculated drag coefficient, the grid-independence is completed.

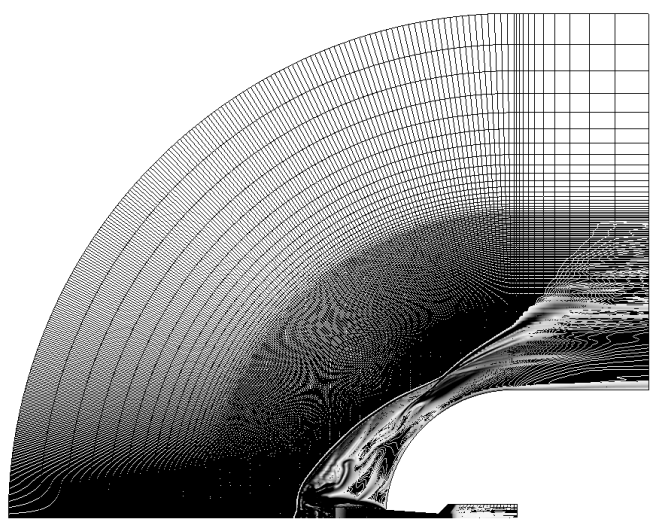

Fig. 11 Grid dependence test of nodes=60000

3.2 Effect of pressure conditions of the jet

To investigate the effect of ideal gas of the air jet pressure conditions on drag reduction, at constant free-stream flow pressure condition, injecting jet pressure conditions are varied at nozzle diameter 2.44mm as presented in Table 1. At fixed stagnation pressure and the nozzle area ratio, the calculated momentum parameter ratio depending on the jet pressure condition is shown at Table 1

NPR means the pressure ratio with the nozzle jet pressure ratio to free-stream flow pressure condition. As MPR is proportional to the pressure and the Mach number, high pressure jet can be high momentum jet. This can be said that high pressure jet can release large amount of mass flow rate of the jet.

Table 1 Flow conditions of free-stream and jet condition with air

Free-stream conditions : $M_\infty = 6,\ T_{0,\infty} = 611K, P_{0,\infty} = 689Kpa$		
Jet condition		
M_e	NPR	MPR
2.86	0.20	$0.92*10^{-2}$
	0.40	$1.84*10^{-2}$
	0.50	$2.29*10^{-2}$
	0.75	$3.44*10^{-2}$
	1.05	$4.82*10^{-2}$
	1.20	$5.51*10^{-2}$
	1.50	$6.88*10^{-2}$

3.2.1 Flow features and flow field

According to the penetration length of the jet, it is possible to categorize the flow field to long penetration mode (LPM) and short penetration mode (SPM)

(1) Long penetration mode

Long penetration mode is the penetration length of the jet is long before reaching to critical point of the pressure as shown in the Fig. 12. In this paper, by increasing the pressure, the shock structure is changed and the drag is suddenly increased. Around this pressure, this is called as critical point. Fig. 12(a) shows the present numerical result and Fig. 12(b) represents previous study [5-7].

LPM represents over-expanded jet. Normally, at over-expanded jet, the back pressure is higher than the exit pressure of the jet, the shock structure is formed with expansion wave.

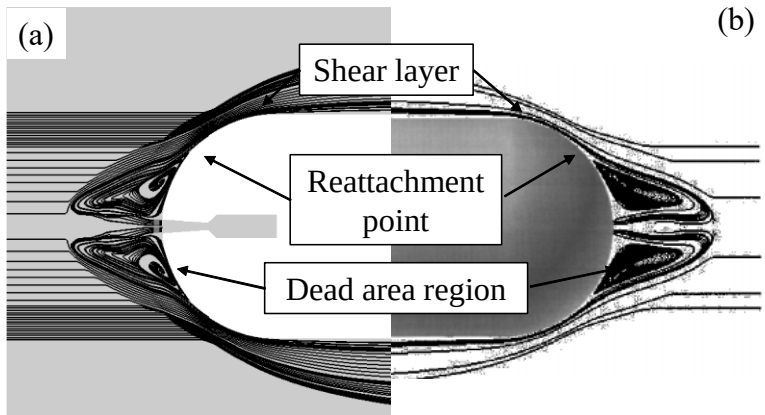

Fig. 12 Analysis of the flow field at LPM (a) Present numerical result (b) Previous study

In this research, the shock structure starts with the expansion wave and is changed from multiple detached bow shock wave to multiple shock wave as shown in the Fig, 12. For LPM, it is possible to investigate three aspects, reattachment point, shear layer and dead area region.

When the jet is coming from the nozzle, some jets penetrate the flow field and interact with the flow field. On the other hand, some other jets retrace back to the blunt body and form dead area region. For counter-flow jet, dead area region is very important role to reduce drag forces. Let's consider the without jet blowing condition. Due to the hypersonic flow, strong bow shock wave is formed in front

of the blunt body and there will be high pressure condition applied on the body nose. However, because of the jet, the dead area region is formed and the high pressure condition is positioned further away from the blunt body nose. In this principle, it is possible to reduce pressure drag. During the shock structure change from bow shock wave to multiple shock structure, the shock is reattached to the blunt body and it is called reattachment point. Moreover, the jet flow retraces back to the flow field and make shear layer. Therefore, in the LPM, three important points are investigated.

For LPM, the shock structure is highly fluctuated so the flow field is very unstable condition. As a result, already mentioned in the above, it is quite difficult to catch the flow field.

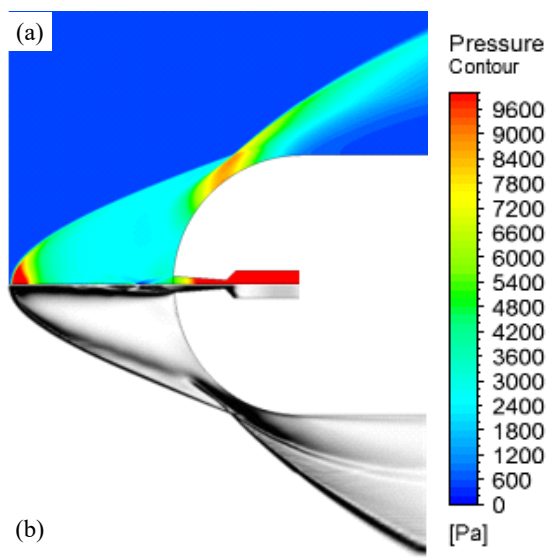

Fig. 13 NPR=0.20 at 1.28ms (a) Local density gradient (b) Pressure contour

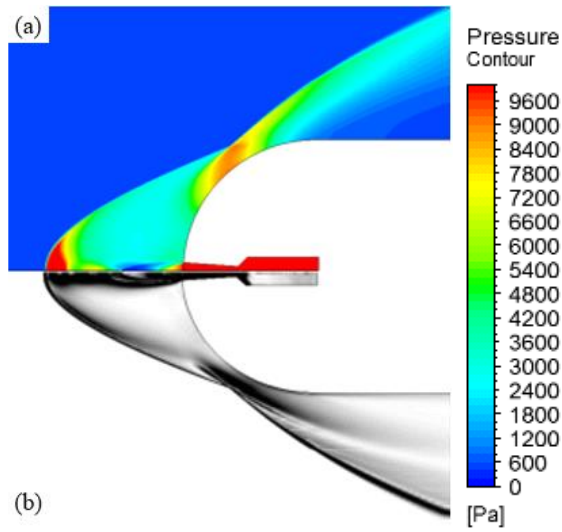

Fig. 14 NPR=0.40 at 0.69ms (a) Local density gradient (b) Pressure contour

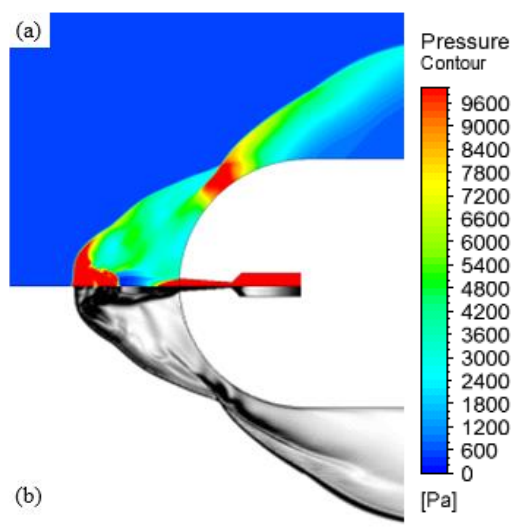

Fig. 15 NPR=0.75 at 0.69ms (a) Local density gradient (b) Pressure contour

Fig. 13-15(a) shows local density gradient and Fig. 13-15(b) represents pressure contour. The contour label is fixed 0 to 15 and the pressure contour line is fixed 0 to 10Kpa to observe the shock structure. Shown in the Fig. 13-15, penetration length of jet is decreasing as the pressure is increasing. At LPM, because the shock structure highly oscillates and the flow field is entirely unstable, the drag could not be significantly reduced even if the penetration length is long.

In addition, the shock structure is quite conical shape and X type of shock structure is investigated. By looking at the pressure contour, reattachment point of shock wave is easily observed and the pressure of the reattachment point is higher than the near area.

(2) Short penetration mode (SPM)

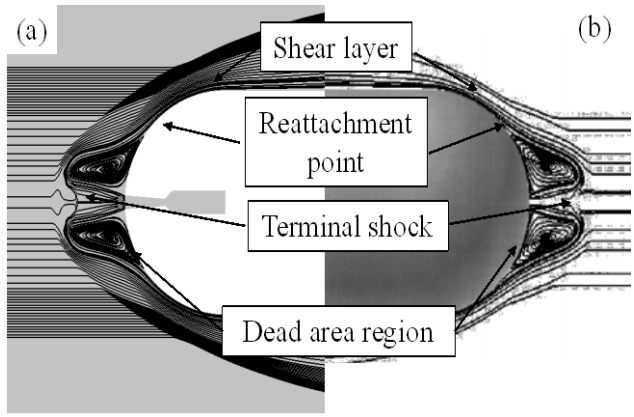

Fig. 16 Analysis of the flow field at SPM (a) Present numerical result

(b) Previous study

Short penetration mode (SPM) means the penetration length of the jet is short after the critical point of the pressure and it can be classified as under-expanded jet. Under-expanded jet means the back pressure is lower than the exit nozzle pressure of the jet so the shock structure starts with compressible shock wave. For SPM, the shock structure is same as LPM as shown in Fig. 16 [5-7]. However, terminal shock is shown. Because of the terminal shock, the penetration length of the jet is not changed and the shock structure is fixed. As a result, the entire flow field of the short penetration mode is stable condition. Moreover, as the shock structure is stable,

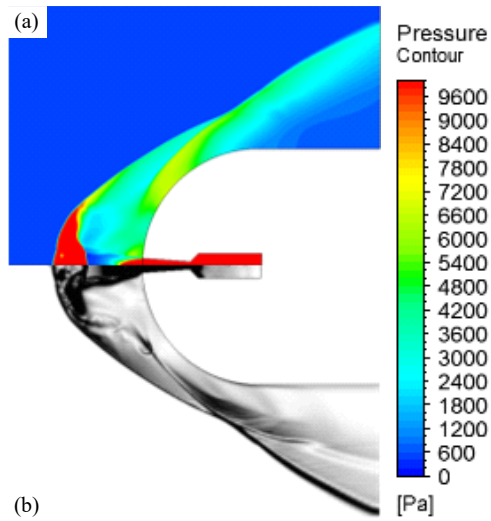

Fig. 17 NPR=1.05 at 0.38ms (a) Local density gradient (b) Pressure contour

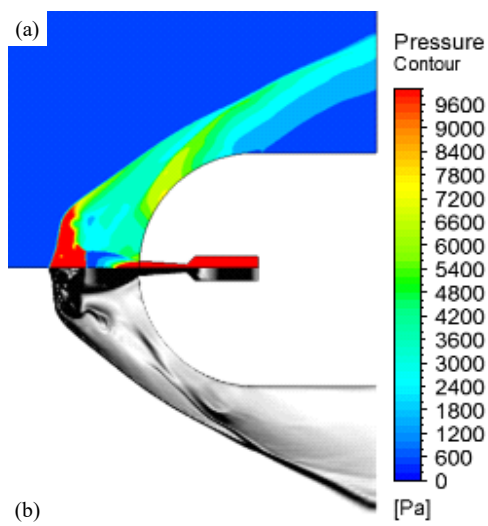

Fig. 18 NPR=1.20 at 0.52ms (a) Local density gradient (b) Pressure contour

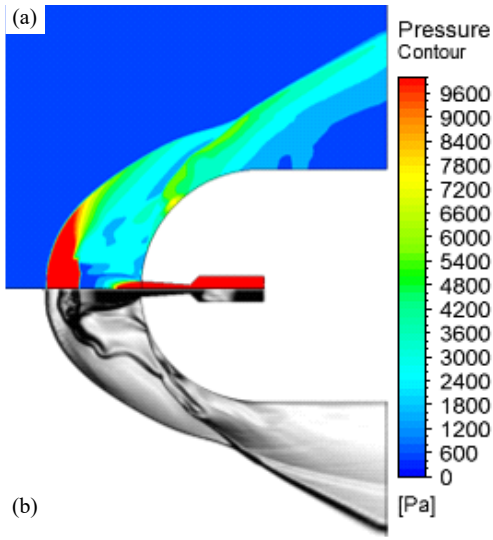

Fig. 19 NPR=1.50 at 0.49ms (a) Local density gradient (b) Pressure contour

Fig. 17-19(a) shows local density gradient and Fig. 17-19(b) represents pressure contour. The contour label is fixed 0 to 15 and the pressure contour line is fixed 0 to 10Kpa to observe the shock structure. Contrary to LPM, as the jet pressure increases, penetration length of jet is increasing and the jet layer is also increasing.

For SPM, the flow field is stable so the drag can be reduced even if the penetration length of jet is short.

3.2.2 Analysis

(1) Drag reduction

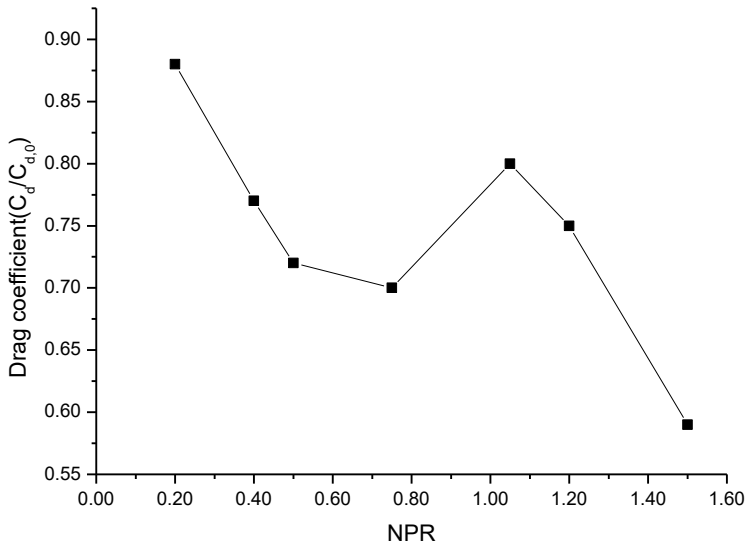

Fig. 20 Total pressure coefficient according to the NPR

Fig. 20 shows the drag coefficient ($C_d/C_{d,0}$) applied on the vehicle body. The drag coefficient of no jet condition and various jet pressure condition is expressed as $C_{d,0}$and C_d respectively. Shown at Fig. 20, the drag continuously decreases until critical point. Critical point means that the shock structure is changed to LPM to SPM. In addition, at critical point, the entire flow field is altered over-expanded jet to under-expanded jet as the jet injection pressure is increasing.

However, over the critical point, the pressure drag suddenly is increasing. This is because of the transition of the jet from over-expanded jet to under-expanded jet. After this critical point, the drag reduces continuously. By changing the pressure ratio, the pressure drag can be reduced approximately 40% compare with the no-jet condition.

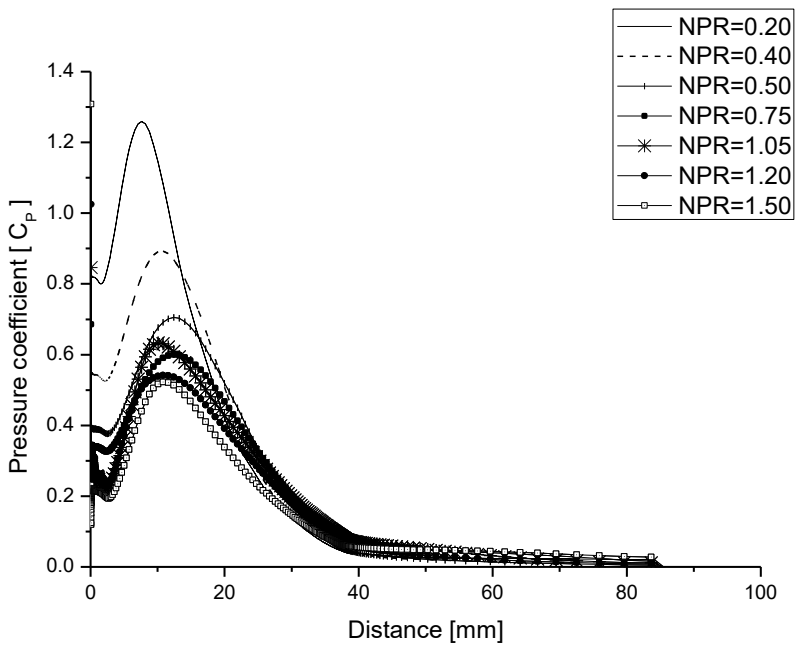

Fig. 21 Wall pressure distribution along the blunt body

Fig. 21 shows the results with the wall pressure distribution alongside the blunt body expressed by pressure coefficient defined by $C_p = \frac{P_j - P_\infty}{\frac{1}{2}\rho v^2}$ and there is a maximum point of the pressure drag coefficient. This point represents the reattachment point of the shock. Depending on the pressure ratio, the reattachment point of the shock is different and is pushed away from the nose of the blunt body as the pressure is increased. The detailed contour line will be discussed later.

Moreover, in the neighborhood of critical point zone, the pressure distribution suddenly increases. This is because not only the transition of the shock wave but also penetration length to the flow field is decreasing. For this reasons, the total pressure coefficient is increasing over the critical point though the mass flow rate of jet is increasing. However, after critical point, as the penetration length becomes longer, the drag is reduced continuously.

3.3 Effect of exit Mach number

To investigate the effect of the jet exit Mach number, at fixed nozzle throat size, the diameter of the nozzle exit is changed as shown in the Table 2. The jet exit Mach number is depended on the area ratio, nozzle jet exit diameter to nozzle throat diameter. In order to ignore the expansion rate of the nozzle, nozzle expansion angle (α) is fixed at 4° as shown in Fig. 5. Lower base selection of lower exit Mach number is same as in the Chapter 3.2. For the other case where higher Mach number is selected as the NPR is 0.20, 0.75, 1.05 and 1.20 when the free-stream pressure is 689KPa. The calculated MPR is presented at Table 3.

Table 2 Parameters of jet

	Lower Mach number	Higher Mach number
Gas species	Air	
$T_{0,j}$ [K]	294	
D_t [mm]	2.44	
α [°]	4	
D_m [mm]	76.2	
M_e	2.86	3.13
A_e/A_t	3.71	4.80

Table 3 MPR at different Mach number

NPR	Lower Mach number	Higher Mach number
0.20	$0.92*10^{-2}$	$0.95*10^{-2}$
0.75	$3.44*10^{-2}$	$3.56*10^{-2}$
1.05	$4.82*10^{-2}$	$4.98*10^{-2}$
1.20	$5.51*10^{-2}$	$5.69*10^{-2}$

3.3.1 Flow features and flow field

Fig. 22 Local density gradient at higher Mach number of jet

(a) SPM at NPR=0.20 (b) LPM at NPR=1.05

In order to compare with the numerical result suggested at Chapter 3.2, the representative NPR is 0.20 and 1.05. Already mentioned, depending on the pressure injection, the flow field is categorized SPM and LPM. The Fig. 22 shows the local density gradient for higher Mach number of jet. Fig. 22(a) represents SPM when NPR is 0.20 and the Fig. 22(b) shows LPM when the NPR is 1.05

Despite the exit Mach number of the jet goes higher, the shape of entire flow field is not changed when compared with Fig. 15-17 as shown in the Fig. 22. On the other hand, presented in Fig. 22(b), the penetration length of the jet is short and because of the jet retrace back to the blunt body, there a few of the jet vortexes are observed.

3.3.2 Analysis

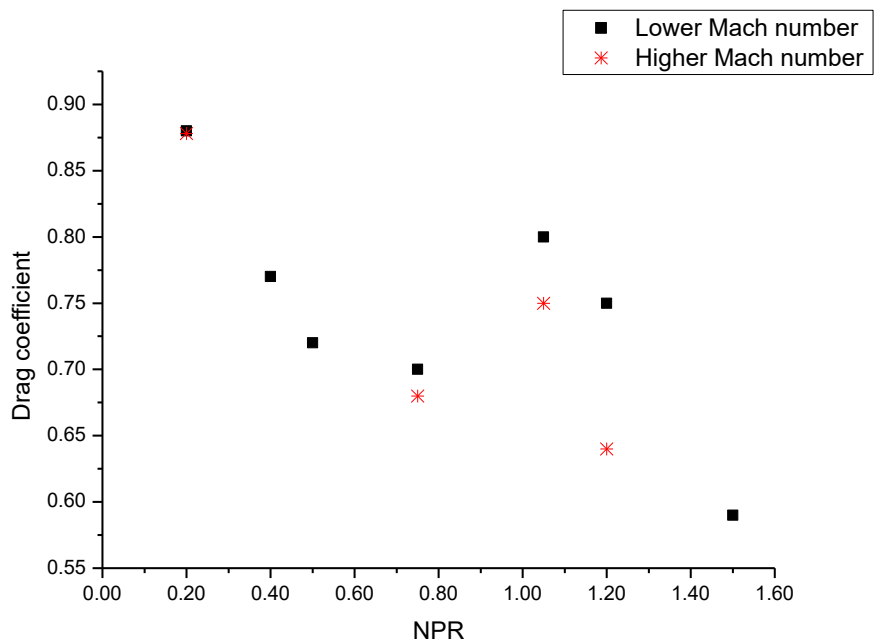

Fig. 23 Drag coefficient for lower Mach number and higher Mach number

The Fig. 23 shows the drag coefficient for lower Mach number and higher Mach number. As shown in the figure, at higher Mach number of the jet, the drag is reduced maximum 5 percent more than the lower exit Mach number. This is

because the MPR is bigger and mass flow rate for higher Mach number of jet than lower Mach number of jet.

3.4 Effect of jet species

It is necessary to investigate what kind of gas species efficient to reduce drag component. To identify the effect of the gas species such as monoatomic, diatomic and polyatomic molecule gas species are used. Ultimately, it means that different gamma ratio of the jet is used. The representative monatomic gas is used in this paper is argon. The diatomic gas is air and the polyatomic molecule gas is carbon dioxide. Air, carbon dioxide and argon is easily obtained at the atmosphere. Moreover, even if these gases release into the air, there are no harmful environmental factors. Therefore, in this paper, argon, carbon dioxide and air are selected. The gas characteristics and details are shown at Table 4.

At different species of the jet, the free-stream flow of the condition is pressure is 689KPa (same as 100 psi), temperature is 611K and the exit Mach number of the jet is 2.86. Already investigated, at under-expanded jet, entire flow field is stable and the drag reduces effectively. Therefore, the different gas species numerical simulation researches conducted at under-expanded jet.

Table 4 Jet flow conditions with different species of jet

	Argon	Carbon dioxide	Air
$\dot{m}\ [g/s]$	9.5	9.1	7.6
$P_{0.j}$ [Kpa]	689		
$T_{0.j}$ [K]	294		
D_t $[mm]$	2.44		
MPR	$6.03*10^{-2}$	$4.59*10^{-2}$	$3.81*10^{-2}$

3.4.1 Flow features and flow field

Fig. 24 shows the local density gradient with different gases. As the computational study was carried out under-expanded jet, all of the flow field is SPM. As shown in the figure, the jet spread out further at higher molecular weight of the jet. In addition, the penetration length of carbon jet is longest than others.

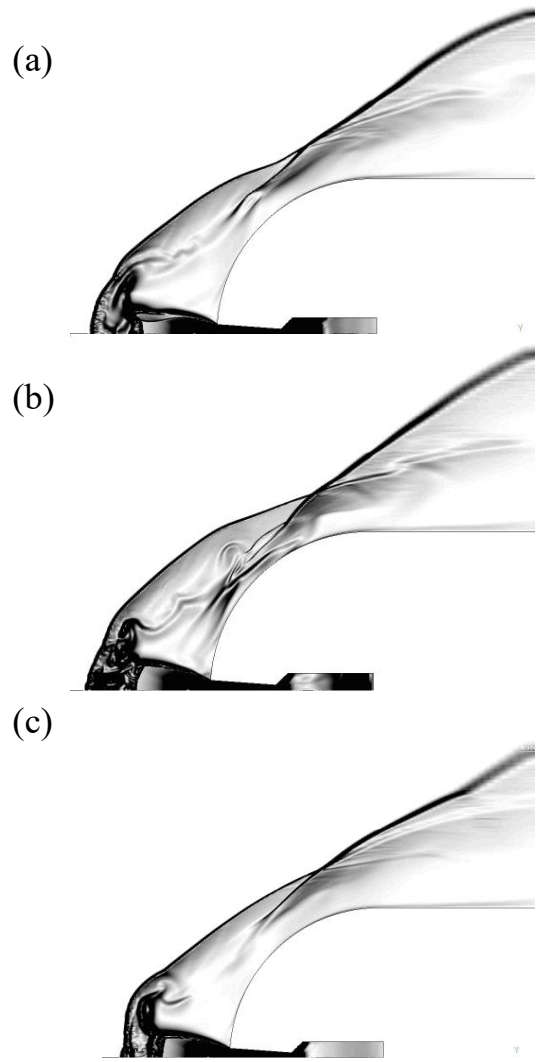

Fig. 24 Local density gradient with different gases

(a) Argon (b) Carbon dioxide (c) Air

3.4.2 Analysis

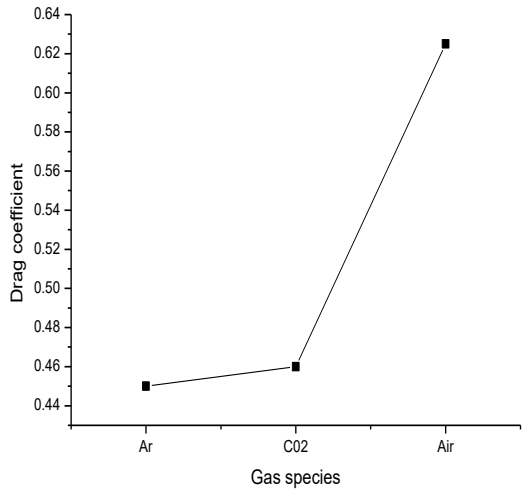

Fig. 25 Drag coefficient with different gas species

At different gas species, molecular weight of argon, carbon dioxide and air is 40, 44, 28.95kg/kmol, respectively. At same jet pressure condition, from the drag coefficient, higher molecular weight of the jet is more efficient than light gas as shown in the Fig. 25. When using the argon gas for counter-flow jet, drag can be reduced up to 50%. This is because of the momentum ratio of the jet. As the MPR is proportional to the gas species, at higher molecular weight of gas, momentum of gas is higher than the lower gases at constant jet pressure. Therefore, higher molecular weight and polyatomic molecule gas is more efficient than the monoatomic, diatomic gases when compared with the calculated MPR.

4. Conclusion

In this paper, three parameters to decide the counter-flow jet are investigated. One point is the jet pressure and the other one is jet Mach number. The last point is jet gas species that different molecular weights.

According to the effect of the pressure injection, as the increasing the pressure of the jet, the flow field could be categorized SPM and SPM depending on the jet penetration length of the jet. Before the critical point of the jet, entire flow field is LPM and the flow field is unstable. Thus, the shock oscillates and fluctuates. From this reason, even if the jet interacts deeply with the free-stream flow, the drag does not been reduced. However, after the critical point, the jet becomes stable condition and the drag can be reduced maximum 40% when compare with the without blowing condition at room temperature of the jet. In addition, because of the momentum of jet, the drag is reduced more than 5% than the lower Mach number. By using argon gas, the drag can be reduced by 60% and carbon dioxide jet is efficient than argon when comparing with the calculated MPR.

From this research, using high pressure ratio, high Mach number and higher molecular weight of jet is beneficial to drag reduction.

5. References

[1] Finely, P. J., “The flow of a jet from a body opposing a supersonic free stream”, Journal of Fluid Mechanics, Vol. 26, 1966, pp. 377-368

[2] Feszty, D., Badcock, K. J., Richards, B. E., “Driving mechanisms of high-speed unsteady spiked body flows, part1: Pulsation mode”, AIAA Journal, Vol 42. 2004, pp.95-106

[3] Panaras, A. G., Drikakis, D., “High-speed unsteady flows and around spiked-blunt bodies”, Journal of Fluid Mechanics, Vol.632, 2009, pp.69-96

[4] Mahapatra, D., Sriram, R., Jagadeesh. G., “Shock tunnel studies on drag reduction of a blunt body using argon plasma jet”, 47th AIAA Aerospace Sciences Meeting Including The New Horizons Forum and Aerospace Exposition, 2009

[5] Shang, J. S., Hayes, J., Wurtzler, K., “Jet-spike bifurcation in high speed flows”, AIAA Journal, Vol. 39, No. 6, 2001, pp. 1159–1165

[6] Shang, J. S., “Plasma injection for hypersonic blunt-body drag reduction”, AIAA Journal, Vol. 40, No. 6, 2002, pp.1178-1186

[7] Shang, J. S., Hayes, J., Menart, J., “Hypersonic flow over a blunt body with plasma injection”, Journal of spacecraft and rockets, Vol.39, 2002, pp.577-591

[8] Bodonoff, S. N., Vas, L. E., “Preliminary investigations of spiked bodies at hypersonic speeds”, Journal of the aerospace sciences,1959, Vol.26, pp.65-74

[9] Osuka, T., Erdem, E., Hasegawa, N., Majima, R., Tamba, T., Yokota, S., Sasoh, A., Kontis, K., “Laser energy deposition effectiveness on shock-wave boundary-layer interactions over cylinder-flare combinations”, shock wave, Vol.26, 2014.

[10] Chamberlain, R., Dang, A., McClure, D., “Effect of exhaust chemistry on reaction jet control,” AIAA Paper 99-0806, Jan. 1999.

[11] Ambrosio, A., Wortman, A., “Stagnation point shock detachment distance for flow around spheres and cylinder”, ARS Journal, Vol. 32, No. 2, 1962, pp.281

초 록

본 논문은 마하수 6 이상의 극초음속으로 비행하는 무딘 물체에 역분사 제트가 항력감소에 미치는 영향에 대한 전산해석적 연구이다. 수치해석 계산을 위하여 2 차원, explicit, 축대칭의 Reynolds-Averaged Navier Stokes (RANS) 방정식이 사용되었다. 또한, 난류를 해석하기 위하여 Spalart-Allmaras one equation 을 이용하였다. 역분사 제트가 자유류 유동으로 흘러감에 따라 기존의 bow-shock 이 다중의 충격파 형태로 변화하게 된다. 이러한 충격파의 변화는 궁극적으로 항력감소를 유도한다. 이에 본 연구에서도, 제트의 모멘텀에 영향을 미치는 Momentum parameter ratio (MPR)를 기반으로 하여 제트의 압력, 제트의 출구 마하수, 제트의 분사기체 종류에 따른 효과를 조사하였다. 본 수치해석적 결과에 의하면 제트의 침투길이에 따라 유동을 크게 Long penetration mode (LPM)과 Short penetration mode (SPM)으로 나뉠 수 있다. 또한, 항력은 최대 40%이상 감소하는 것으로 조사가 되었으며 높은 출구 마하수의 제트가 낮은 출구 마하수의 제트보다 5% 이상 항력을 감소시킨다. 분사기체를 바꾸어서 시행해본 결과, 분자량이 가장 높은 아르곤에서 항력이 60%이상 감소하였으며, 분자량이 높을수록 효과가 좋은 것으로 계산이 되었다.

따라서, 본 연구를 통하여, 압력이 높을수록, 출구 마하수가가 클수록, 제트의 분자량이 무거울수록 항력감소에 효과적인 것으로 계산이 되었다.

주요 단어 : 극초음속, 역분사 제트, 항력감소, Momentum parameter ratio(MPR)

학 번 : 2015-20783